Trace element volatility and the conditions of liquid-vapor separation in the proto-lunar disk

Dmitry Ivanov, Caroline Fitoussi, Bernard Bourdon

Icarus 386 (2022) 115143

Contents lists available at ScienceDirect

Icarus

journal homepage: www.elsevier.com/locate/icarus

Trace element volatility and the conditions of liquid-vapor separation in the proto-lunar disk

Dmitry Ivanov [1], Caroline Fitoussi, Bernard Bourdon [*]

Laboratoire de Géologie de Lyon, ENS Lyon, CNRS, Université Claude Bernard de Lyon, 46 Allée d'Italie, 69364 Lyon cedex 07, France

ARTICLE INFO

Keywords:
Moon
Giant impact
Condensation
Protolunar disk
Volatile trace elements

ABSTRACT

The Moon is thought to have formed from material ejected by a giant impact that took place at the end of Earth's accretion. The material ejected to space generated a large hot structure where material beyond the Roche limit accreted to form the Moon. It has long been known that the Moon is characterized by abundances in moderately volatile elements (MVE) lower than that of the Earth, while more recent studies have established that the concentrations in refractory elements are similar to the bulk Silicate Earth. The thermodynamic conditions that prevailed after this impact are poorly known and understanding the origin of the Moon-Earth differences in MVE requires a knowledge of the volatility of elements under these conditions. In this study, we reexamine the volatility of a large set of geochemically relevant elements and attempt to determine the P-T conditions under which volatiles were putatively separated from the liquid material. Our model predicts very different condensation temperatures due to higher pressures, compared with the conditions of the Solar Nebula and we extend the values of these temperatures to a wide number of trace elements (Se, Ag, Pt, Mo, W, Zn, Sn, Sb, Rb, Cs, U, Th, Cr, Ni, Co, Ga, Ge, Cu, and P). Our modeling shows that the observed lunar compositions cannot be explained by a single set of P and T conditions. Rather, it is best explained by a mixture between high-temperature condensates (~4000 K) and low temperature condensates (2000-2500 K). An important constraint is that for the low temperature condensates, liquid metal must have been stable and this is crucial for matching the abundance of volatile siderophile elements in the bulk Moon.

1. Introduction

Lunar exploration programs have revealed that the composition of the Moon is depleted in moderately volatile elements compared with that of the Earth. Notably, the K/Th ratio of the bulk silicate Moon is lower than the estimated value for the bulk silicate Earth (e.g., Hauri et al., 2015; O'Neill, 1991; Prettyman et al., 2006; Taylor and Wieczorek, 2014). This critical observation has been one of the arguments in favor of the formation of the Moon by a giant impact. Following the impact, the ejected material forms a disk of debris that later reaccretes to form the Moon. The physical state of the disk depends on the size of the impactor and on the nature of the collision. It has been shown by Nakajima and Stevenson (2014) that the initial mass fraction of vapor in the disk could be very variable. For canonical impacts (e.g., Canup, 2004) involving a Moon to Mars-size object colliding obliquely with the Earth (Canup, 2008), the mass fraction of vapor is rather low. For these impacts, the impactor represents 60 to 80% of ejected material, a conclusion that seems at odds with observations that Cr, Ti and O isotopes are almost identical in the Moon and the Earth (Mougel et al., 2018; Young et al., 2016; Zhang et al., 2012). More recent models have shown that with non-canonical impacts involving for example a fast-spinning Earth (Ćuk and Stewart, 2012) or a much larger impactor size (Canup, 2012), the mass fraction of vapor can be much higher and the ejected material has more or less the composition of the bulk silicate Earth, in better agreement with observations. A particularity of these types of impacts is that the angular momentum (AM) of the Earth-Moon system has to be higher than that of the present-day. This requires a mechanism to lower the initial high AM and several processes have been suggested (Cuk et al., 2016; Ćuk and Stewart, 2012; Tian et al., 2017; Wisdom and Tian, 2015; Cuk et al., 2016; Rufu and Canup, 2020). It was then shown by Lock et al. (2018) and Lock and Stewart (2017) that these high AM and high energy impacts could generate specific structures called synestia that include both a corotating region and a disk-like region above the corotation limit (defined as bodies with a constant

* Corresponding author.
E-mail address: bernard.bourdon@ens-lyon.fr (B. Bourdon).
[1] Now at: Astrophysics Lab, Columbia University, New York, USA.

https://doi.org/10.1016/j.icarus.2022.115143
Received 1 July 2021; Received in revised form 15 June 2022; Accepted 16 June 2022
Available online 21 June 2022

Table 1
BSE starting composition.

Element	%wt.	Element	ppm	Element	ppb
O	44	Na	2670	Ga	4000
Mg	22.8	Cr	2625	Ge	1100
Si	21	Ni	1960	Rb	600
Fe	6.26	Ti	1205	Sn	130
Ca	2.53	Mn	1045	Th	79.5
Al	2.35	S	250	Se	75
		K	240	Mo	50
		H	0–1000	W	29
		C	120	Cs	21
		Co	105	U	20.3
		P	90	Ag	8
		Zn	55	Pt	7.1
		Cu	30	Sb	5.5

Table 2
Activity coefficients for the trace elements in silicate melts.

Component	Activity coefficient, γ	Temperature	Reference
$AgO_{1.5}$	0.066	1973	(Norris, 2016)
MoO_2	0.003	1973	(Norris, 2016)
$SbO_{1.5}$	1.9	1973	(Norris, 2016)
WO_3	0.064	1973	(Norris, 2016)
K_2O	4.84×10^{-8}	1673	(Sossi et al., 2019)
Rb_2O	1.69×10^{-8}	1673	(Sossi et al., 2019)
Cs_2O	6.0×10^{-9}	1673	N/A

Table 3
Activity coefficients for some trace elements in liquid metal.

Element	Activity coefficient, γ	Temperature (K)	Reference
Ag	200	1873	Steelmaking source book (1988)
Ga	1	1873	Steelmaking source book (1988)
Ge	0.0354	1873	(Wood et al., 2019)
Pt	0.022	1873	(Wood et al., 2019)
Se	0.01	1873	(Schuster et al., 1979)
Sb	1.36	1873	(Tsukihashi et al., 1994)
W	1	1873	Steelmaking source book (1988)

angular velocity).

The thermodynamic conditions in the post-impact structures set the initial stage for the chemical evolution of protolunar disk or synestia. However, there are several scenarios based on these various structures for explaining volatile element loss during this evolution. In the models based on the canonical impacts, the possibility of hydrodynamic escape of volatiles was discussed (Machida and Abe, 2004), but it was shown later that this mechanism could not lose elements heavier than hydrogen (Nakajima and Stevenson, 2018). Another possibility was that the loss of volatile elements was due to incomplete condensation of the vapor to the Moon followed by the fall back of residual vapor to Earth, leading to volatile depletion in the accreted moonlets (Canup et al., 2015; Charnoz and Michaut, 2015; Lock et al., 2018). However, the three considered scenarios were not identical in details as the process behind vapor-melt decoupling differed. Canup et al. (2015) argued that the melt condensing within the inner disk would be volatile-poor and this melt would feed the outer disk, and become incorporated into the accreting Moon, while part of the accreted material in the outer disk did not involve such a decoupling. With this scenario, the overall degree of volatile depletion would depend on the mixing proportions of inner disk and outer disk melts within the accreted Moon. Charnoz and Michaut (2015) showed that the decoupling between vapor and melt could take place, provided there was an effective viscosity of the vapor phase. This viscosity is likely to be high enough, only if there is enough ionization in the disk (Gammie et al., 2016), but this parameter is in fact poorly constrained. Lock et al. (2018) have modeled the effect of heating and rotation in the large structure surrounding the Earth and concluded that melt could also decouple from vapor as the vapor is being drained towards the Earth, while moonlets can stay on keplerian orbits. Last, Charnoz et al. (2021) modeled the effect of the tidal pull of the Earth on the atmosphere above the lunar magma ocean and argued that the predicted flux could account for the volatile element depletion in the Moon. It remains unclear whether such a model can explain the isotope differences between the Earth and the Moon (see Tang and Young, 2020).

An explicit model for Moon formation should have a strong thermodynamic basis. Previous studies (Canup et al., 2015; Lock et al., 2018) have calculated the condensation temperatures for a limited number of elements using the pressure and temperature conditions that were derived from a physical model. These calculations revealed clearly that the condensation temperatures determined for the Solar Nebula are not identical to those that controlled lunar formation for several reasons: (1) the H_2 dominated vapor phase is no longer present; (2) the bulk composition in major elements is different from that of the Sun with a notably lower amount of iron metal; (3) the redox conditions that control element volatility are more oxidizing due to the low abundance of H_2 and C which are both depleted in the bulk silicate Earth. It was determined by Albarède et al. (2015) that a proxy for condensation temperature was the bond energy and these authors showed that the depletion in volatile elements in the Moon relative to the Earth followed a trend when elemental abundances were plotted as a function of their bond energies. More recently, Lock et al. (2018) recalculated the condensation temperatures using a BSE composition including Mn, Cu, K, Na, Zn and Ge and showed that the lunar abundances could be reproduced for melt-vapor equilibrium temperature above 3465 K corresponding to pressures above 10 bars approximately but this study also showed that a wider range P-T conditions could also match the observations (see the electronic supplement of Lock et al. (2018) for example). Our study was an attempt to revisit these questions using more elements to explore whether one could provide tighter constraints on the P-T conditions of vapor-melt separation.

The observations of isotopic differences between Moon and Earth in volatile elements have further complexified this picture, as the enrichment in heavy isotopes in the Moon for several volatile elements (Zn, Rb, Ga and K) has been interpreted both by condensation during evolution of the proto-lunar disk (Wang and Jacobsen, 2016) or by partial evaporation during a magma ocean stage (Kato et al., 2015; Kato and Moynier, 2017; Paniello et al., 2012; Pringle and Moynier, 2017). A third explanation proposed by Nie and Dauphas (2019) was that the enrichment in heavy isotopes in the Moon could be explained by evaporation under conditions of near equilibrium with vapor being drained towards the Earth due to the viscous properties of the disk as described in several studies (Carballido et al., 2016; Charnoz and Michaut, 2015; Gammie et al., 2016).

In contrast, Sn and Cr isotopes (Sossi et al., 2018; Wang et al., 2019) have revealed an enrichment in light isotopes in the condensed phase (i.e. the Moon), which questions an origin due to kinetic effects during evaporation in a magma ocean context (Day and Moynier, 2014; Dhaliwal et al., 2018). This latter interpretation was further questioned by Tang and Young (2020) who argued that no isotope fractionation should be observed during magma ocean volatile loss. Understanding better these observations clearly requires more constraints on the vapor-liquid thermodynamic equilibrium, as well as the speciation of trace elements in these conditions.

Our goal in this study is to revisit the liquid-vapor equilibrium during the Moon-forming event to examine whether the volatile element depletion could indeed be explained by volatilization during the protolunar disk stage and to gain more constraints on the P-T conditions of melt-vapor separation. Another goal was to explore more extensively the

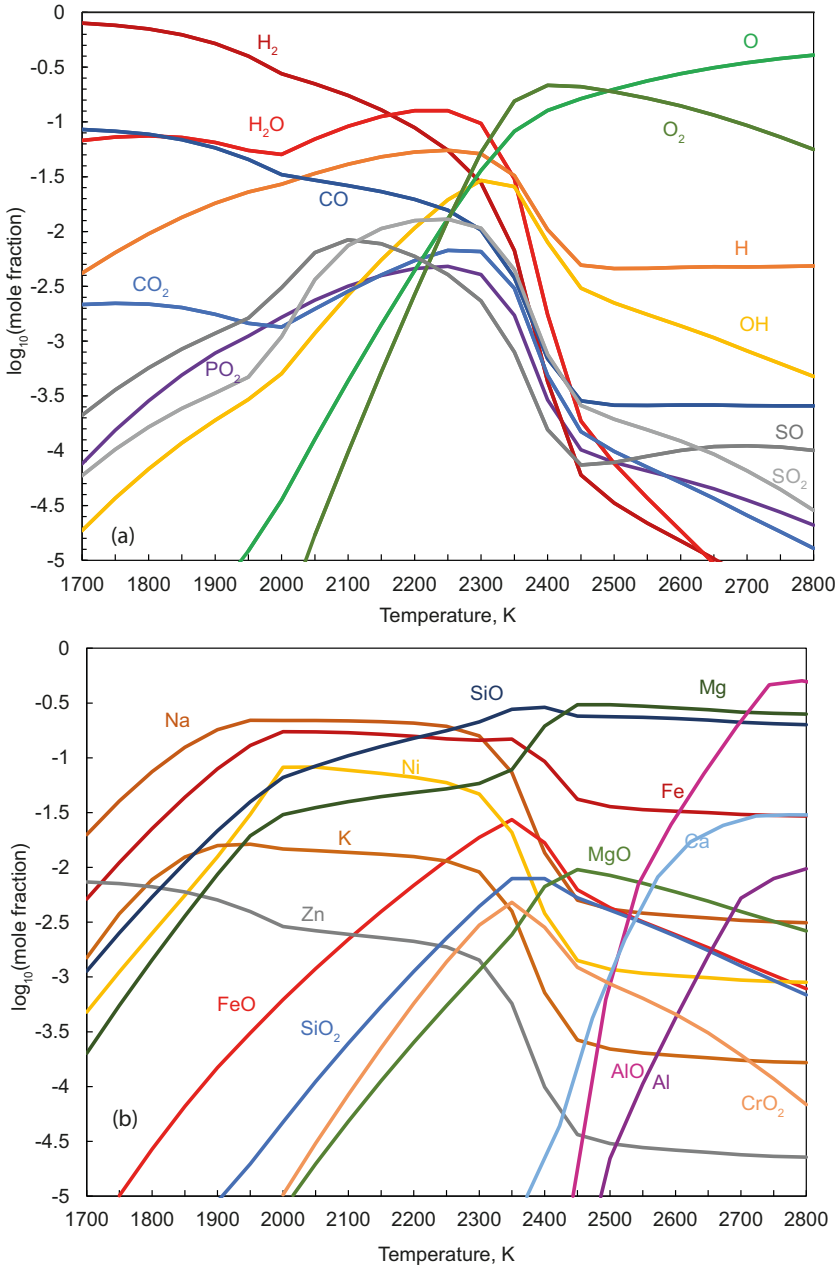

Fig. 1. Composition of the saturated vapor over BSE melt as a function of temperature for a pressure of 1 mbar (a) non-metal species (b) metal containing species.

thermodynamic conditions that would lead to the observed volatile element depletion in the Moon relative to the Earth, in particular, by exploring a wider range of P-T conditions and more trace elements than those used in previous studies (Canup et al., 2015; Lock et al., 2018) for comparing the Moon and Earth compositions.

2. Methodology

2.1. Choice of starting composition

In order to model the chemical equilibrium between the vapor and melt during the formation of the Moon, one needs to make assumptions about the initial bulk composition of the system. A logical choice made by previous authors (Canup et al., 2015; Lock et al., 2018; Visscher and Fegley, 2013) is to consider the bulk silicate Earth (BSE) as the material that got vaporized during the Moon-forming impact. In this study, we have chosen the BSE composition given by McDonough and Sun (1995). All the elemental abundances were expressed as moles and the abundance of oxygen was calculated to obtain the corresponding oxides (e.g. Al_2O_3, SiO_2, FeO), such that there is no excess Fe or Ni metal in the BSE composition. A critical element is hydrogen since the water content of the Moon is a matter of debate (Albarède et al., 2015; Hauri et al., 2015; O'Neill, 1991; Pahlevan et al., 2016). Thus, one of our objectives was also to examine whether water could have an influence on the volatility of some elements, which can form hydroxides in the vapor phase. The corresponding H contents in the bulk material ranged between 0 and 1000 ppm, with the default value at 200 ppm.

2.2. Thermodynamic modeling of volatile elements

Our approach was then to determine chemical equilibrium by specifying the bulk chemical composition, the pressure and the temperature of equilibrium using the FactSage software (Bale et al., 2016) with the FactPS, FToxid, FTsalt and FSstel thermodynamic data bases. These data

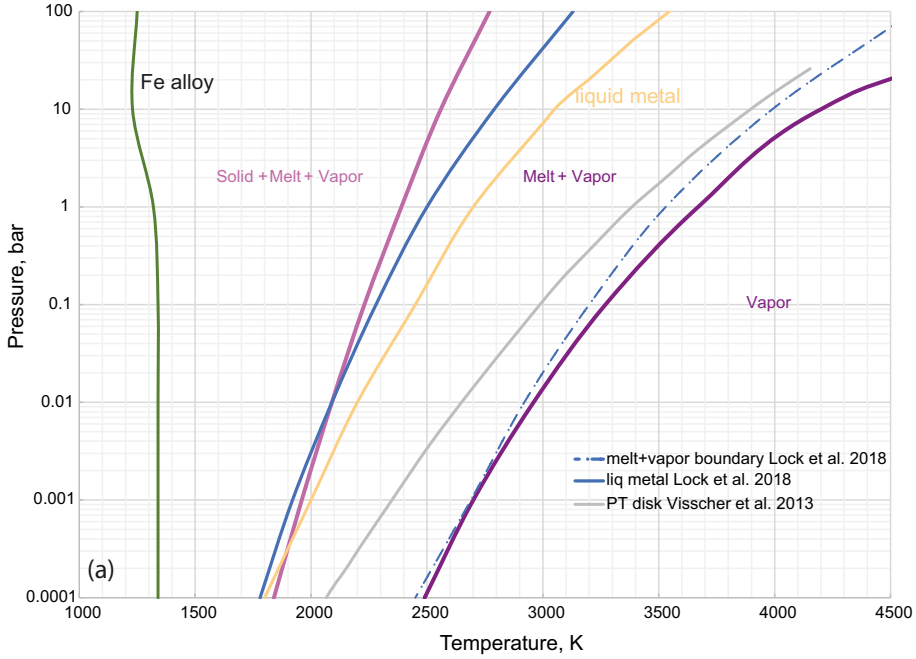

Fig.2. (a) Pressure-temperature phase diagram for the BSE composition. Purple solid lines were determined in this study and indicate the boundaries between vapor and vapor+melt and vapor+melt and vapor+melt+solid phases. Blue lines correspond to the phase boundaries taken from Lock et al. (2018). Green line shows the appearance Fe metal in a solid state. The grey line corresponds to the P-T of the BSE disk given in Visscher and Fegley (2013). The yellow line shows the appearance of the liquid metal phase. (b) Pressure-temperature phase diagram for the BSE composition calculated in this study together with lines indicating the vapor fraction. Vapor fractions are indicated next to each curve. (c) Bulk condensation curves as a function of pressure. The curves are labeled with pressures given in bars. (For interpretation of the references to colour in this figure legend, the reader is referred to the web version of this article.)

bases include a large number of gaseous compounds, solids with numerous solutions relevant to planetary science as well as solution models for molten iron metal, molten oxide mixtures and sulfides (See Table S1 for details). The following elements whose abundance is given in Table 1 were used for the calculations.

For the molten oxides, the FToxid-[SLAGA] mixtures were used as this includes the largest number of elements, while for the metals the FT-Stel-Liquid data base was included. The chemical equilibrium was calculated for various values of the pressure ranging between 100 and 10^{-3} bars and at each pressure, chemical equilibrium was calculated with 50 K temperature steps to obtain the condensation curves and with 10 K intervals for the phase diagram. At each T and P conditions, the number of moles and mole fractions of each constituent in the identified stable phases were calculated. By summing the number of moles of each species both in the gas and condensed phases, it is possible to calculate the fraction of condensed material as a function of temperature and pressure.

2.3. Activities of moderately volatile elements in silicate melts and liquid metal

For a limited number of trace elements, the activity coefficients are not available in the FToxid and FTstel data base (specifically in FToxid-SLAGA). By default, the activity coefficients of these elements would be assumed to be equal to 1, which means that their volatility would not be properly estimated if there are large deviations of the activity coefficients from 1. However, there has been experimental data recently produced (Norris, 2016) for some of these elements at a constant temperature (1973 K) for a range of silicate melt compositions. These activity coefficients were even parameterized as a function of molar abundance of major oxides (e.g. CaO, FeO etc.). For our model we have used the values of these activity coefficients determined for BSE composition and assumed them to follow the relationship:

$$ln(\gamma_i) = \frac{A}{RT}$$

Similarly, we have added the activity coefficients determined by Sossi et al. (2019) for K and Rb, using the same formalism. These activity coefficients are similarly low to those reported by Mathieu et al. (2008) and Abdelouhab et al. (2008). For the case of Cs, whose activity coefficient was not measured by Sossi et al. (2019), we extrapolated it based on the values measured for Na, K and Rb and showed that these values form a linear trend as a function of the ionic radius (Supplementary Information) and with this approach an activity coefficient for Cs (close to that of Rb) could be estimated (Table 2 and see Fig. S1). Overall, the uncertainties in the values of activity coefficients for alkalis warrant dedicated studies in the future. These parameters were introduced into FactSage and this 'solution' model was then merged with the Slag_A model for molten oxide mixtures. Similarly, the activity coefficients of some siderophile elements in molten iron not included in the FT-Stel data base were added as a second solution merged with the liquid iron model (Table 3). This permitted us to refine the calculation of volatility for these elements and to include the most up to date data for silicate melt and liquid metal. It should also be easy to update our modeling as soon as more extensive activity data is produced for these elements.

3. Results

3.1. Major elements and gas phase speciation

The compositions of gas and condensed phases were calculated at each fixed pressure for temperatures ranging between 500 and 3500 K (and up to 4500 K when relevant, see Table S2). The mole fractions of the main metal-containing and non-metallic saturated vapor species calculated at pressure of 1 mbar are depicted in Fig. 1a and Fig. 1b, respectively. The fractions of gas phase products and their temperature

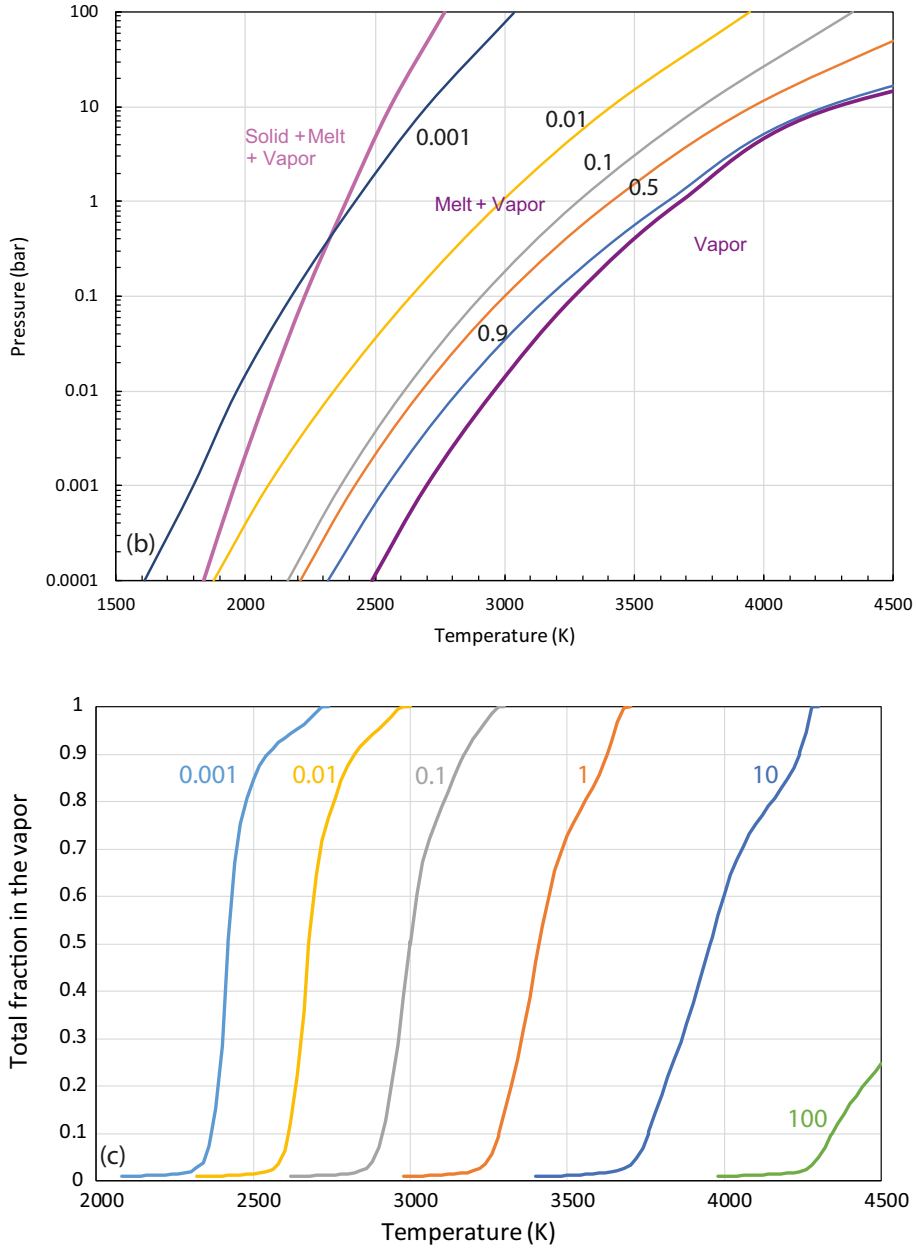

Fig.2. (*continued*).

dependences are similar with those calculated earlier with the MAGMA code (Visscher and Fegley, 2013) for the BSE composition, a notable difference is that our calculations include some water. In the range of temperature reported by Visscher and Fegley (2013) we obtain the same pattern for the most abundance elements in the vapor phase. A more direct comparison with Visscher and Fegley (2013) can be made by considering Fig. S5 where the same input composition for the BSE composition and P-T conditions were used as in Fig. 2a of Visscher and Fegley (2013). The output calculations are similar for Mg, MgO, SiO, SiO_2 but give lower O and O_2 at low temperature, higher K and Ca species and Al species lower than 10^{-5} (mole fraction in the vapor). These results validate our thermodynamic calculations and additional comparison with calculations at higher temperatures by Xiao and Stixrude (2018) are given in the Electronic Supplement (see Fig. S2). As shown in Fig. 1, most metals are stable as the atomic species (e.g. Na, Mg, Fe, K, Ni and Ca) while three of them are more abundant as an oxide species in the vapor (SiO, AlO and CrO_2). Some of the metals are present in both atomic and oxide forms in comparable ratios (Mg/MgO, Fe/FeO). At high temperatures, O_2 is one of the most abundant species among the elements in the vapor phase, while H_2 becomes the most abundant at temperatures below 2150 K and its fraction is higher than for H_2O and CO by an order of magnitude. The large O_2 partial pressure in the vapor phase only prevails at temperatures above 2300 K. Sulfur is present in the vapor phase mainly as SO and SO_2 while it gets dissolved both in the liquid metal and the silicate melt with decreasing temperature. At a pressure of 1 bar, it forms a solid sulfide only below 1100 K. In contrast, H and C remain mostly in the vapor and get dissolved in the metal as the temperature cools down, as the Factsage™ database used here did not include a solution of C and H for silicate melts.

3.2. Phase diagram vapor-melt-solid

The equilibrium composition for the BSE system was calculated for pressures ranging between 10^{-4} and 100 bar, while the temperature range was 500–4000 K. A pressure-temperature phase diagram calculated in this study is shown in Fig. 2 and is overall in agreement with the

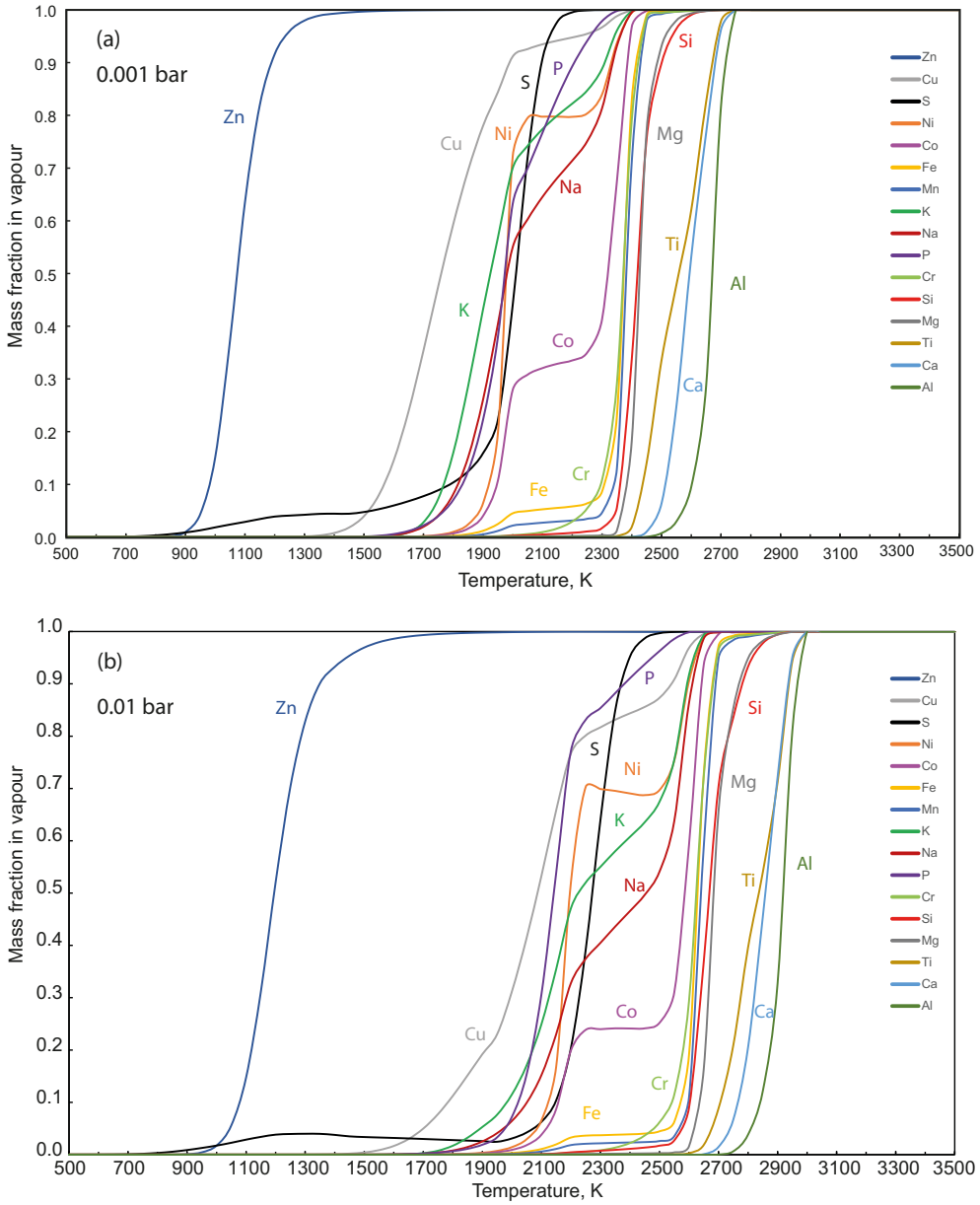

Fig. 3. Condensation curves for BSE composition at different pressures. (a) 0.001 bar (b) 0.01 bar. (c) 0.1 bar (d) 1 bar. (e) 10 bar.

phase diagram obtained by Lock et al. (2018). The line corresponding to the first appearance of liquid metal is also plotted for reference. Iron forms a solid phase at 1340 K (except at pressures higher than 1 bar). Nickel can form NiX solid alloys (X = Ge, S, P, Sn, Se, Sb) at temperatures ranging between 950 K (10^{-4} bar) to 1520 K (10^{2} bar).

3.3. Condensation curves for siderophile and lithophile elements

The condensation curves were calculated for pressures ranging between 10^{-3}–10 bar and for temperatures ranging between 500 and 3500 K (Table S3 containing also the vapor fraction for certain P-T values). For each pressure value, the mass fractions of elements in the gas phase were calculated and then plotted as a function of temperature with 50 K steps. The condensation curves for the most abundant elements in the BSE composition are shown in Fig. 3. With the selected elements, the first elements to condense are Ca, Al and Ti oxides followed by Mg, Si, Mn and Cr. At slightly lower temperatures, Ni, Co and Fe condense as liquid metal. For example, at 10^{-3} bar, liquid Fe—Ni alloy first condenses around 2000 K with 51% wt Ni and 47% Fe. The metal condensation curve is thus offset to slightly higher temperatures than that of Lock et al. (2018) who reported a metal condensation curve around 1900 K. For comparison at 10 bars, the first condensation of metal is around 3050 K with a 52%wt Ni and 40%wt Fe mixture. Thus, the prediction of our calculation is that the first metal forming from the BSE vapor should be Ni-rich. If we then assume that the Moon forms only from the higher temperature condensates, this is consistent with the enrichment in Ni predicted in the lunar core based on siderophile elements in the lunar mantle (O'Neill, 1991). This feature would be unlikely to be observed for a lunar core derived from the core of the impactor because it should have a Ni content more similar to that of other planetary materials such as chondrites and this scenario would also be inconsistent with the low Mo content of the lunar mantle (O'Neill, 1991). For example, adding 1% of impactor's core to the Bulk Moon would boost the bulk silicate Moon to a Mo concentration of 17 ppb, well above

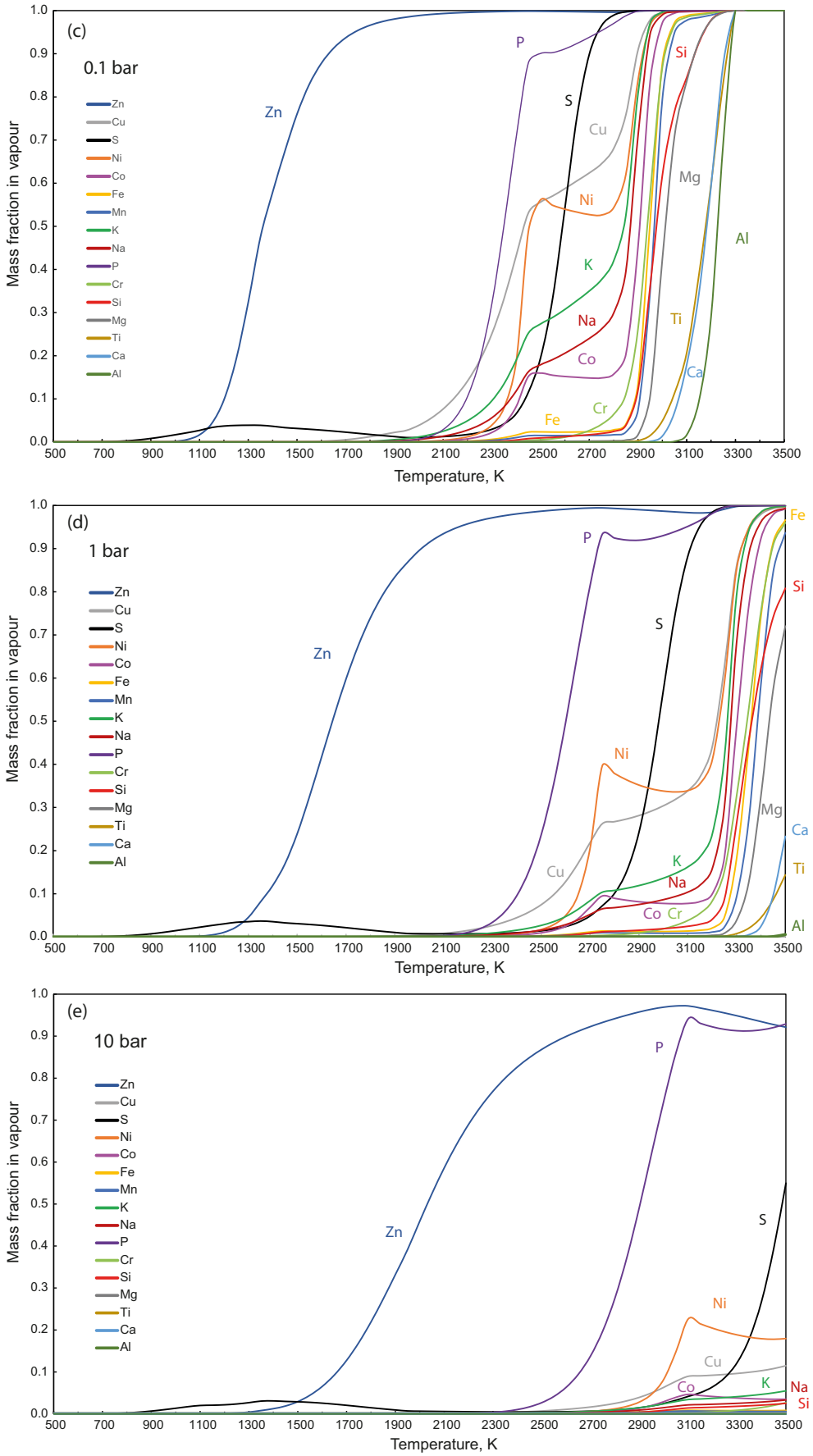

Fig. 3. (*continued*).

Table 4
50% condensation temperatures at 1 bar.

Element	Condensation temperature in K (50%)
Pt	2725
W	3337
Cs	3267
Sb	2201
Sn	2680
Ag	1586
Mo	3385
Rb	2235
Se	2314
Ge	2196
Ga	2644
Zn	1652
Cu	3219
Ni	3228
Co	3306
Fe	3362
Mn	3389
Cr	3346
Ti	3610
Ca	3578
K	3266
S	2983
P	2674
Si	3366
Al	3621
Mg	3438
Na	3278
O	3409

the observed concentration of 2.2 ppb (Hauri et al., 2015).

The condensation temperatures for all the elements at a pressure of 1 bar are reported in Table 4 (see also Table S3 for condensation temperatures at a wider range of pressures). These temperatures are much higher than those reported by Lodders (2003) and Wood et al. (2019) as expected, due to the effect of pressure. Temperatures of condensation are also plotted in Fig. 4 for the volatile trace elements. For the sake of comparison, we also calculated the condensation curves for the same elements with the assumption that these elements have activity coefficients equal to 1 (ideal solutions) and the condensation curves are shown in Fig. S3. There are some significant offsets in the condensation temperatures especially for Mo, W, Se and Ge.

The condensation curves are overall in agreement with those obtained by Lock et al. (2018). For a number of elements, there are some steps in the condensation curves (e.g., Ni and Co). This phenomenon can be explained by the variations in the liquid silicate and metal composition. Transition metals such as Cu, Ni, Co, Fe, and Mn are partitioned between sulfides, oxides and metallic alloys, and as temperature decreases, their activity coefficients in these phase change, thereby causing non-monotonous behaviors during their condensation. In the case of Ni and Co one can observe that the step in the condensation between 2550 and 2200 K is coupled to a greater dissolution of S in the silicate melt which may indirectly affect the activity coefficient of these elements in the melt (Fig. 1a). Another explanation is that this step corresponds to a greater amount of K in the melt that is known to modify the melt structure. Fully understanding these features would require a deeper understanding of the variation of Ni and Co activities in the silicate melt (note that these features can also be observed at higher pressures).

There is a systematic correlation between the condensation temperature of an element and pressure. For pure substances, the condensation temperature is determined by the Clausius–Clapeyron equation which is a function of pressure, vaporization enthalpy and of the difference between the molar volumes of liquid and vapor. As shown in Fig. 5, when one plots the 50% condensation temperatures as a function of pressure, the slopes show smooth variations with an increase in slope at higher temperatures for most elements, except for K, Na, Cu and Ni. The behavior of these curves can be described by a generalized Clausius–Clapeyron equation for a multicomponent solution (Tao, 1969). If the gas phase behaves ideally (which should be the case at low pressures), this suggests that the latent heat of these elements in the mixtures is also rather constant for the elements shown in Fig. 5.

3.4. Speciation of trace elements in the volatile phase

For each trace element, the speciation in the volatile phase was also examined. While the speciation of major elements is already known

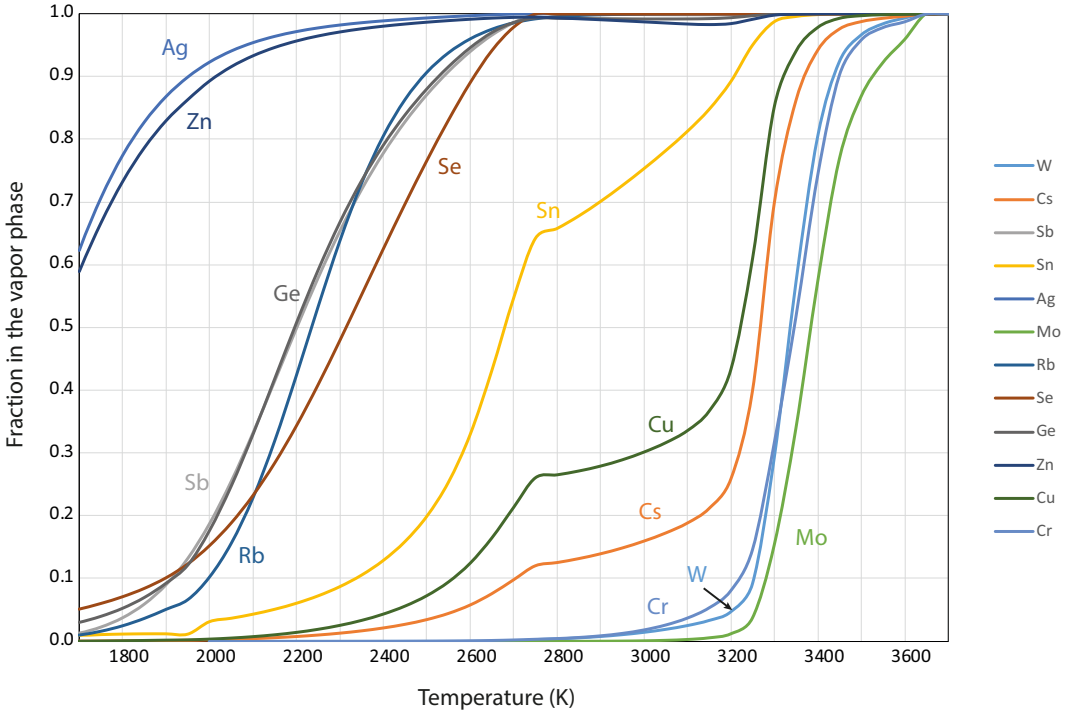

Fig. 4. Condensation curves of trace elements for BSE composition at 1 bar.

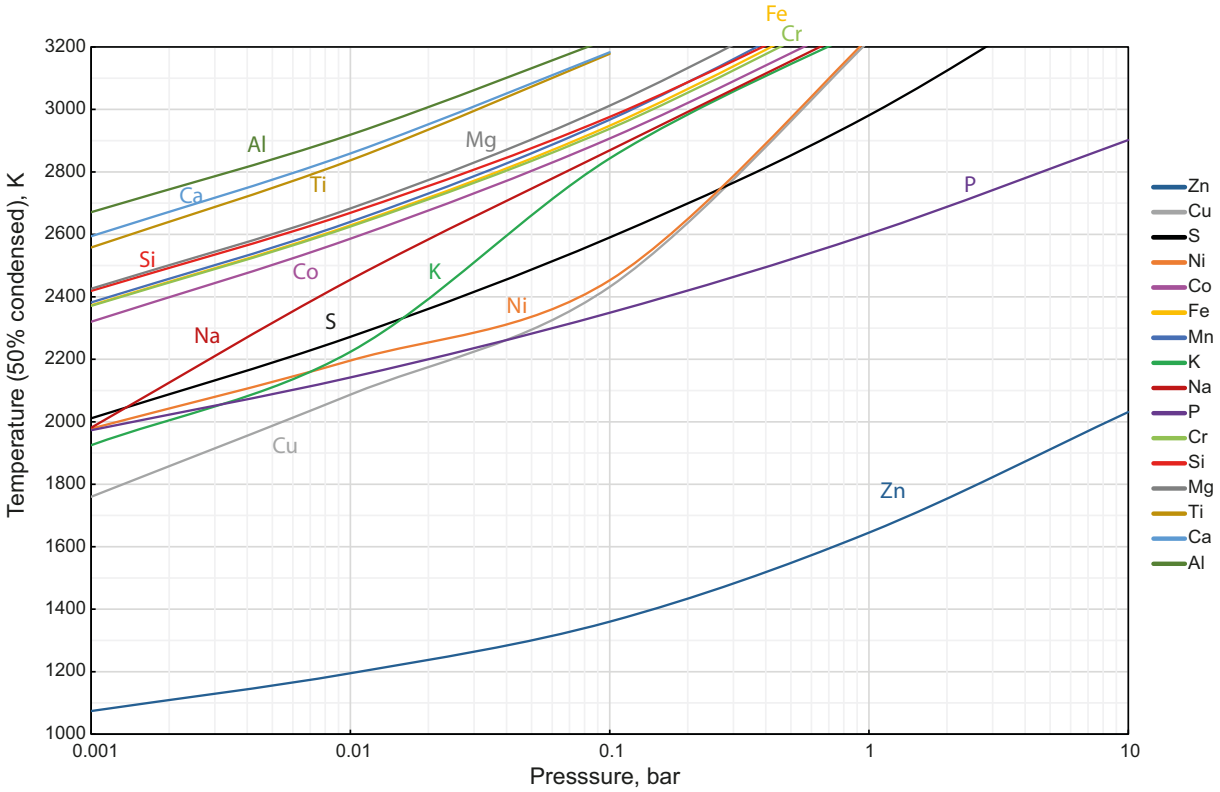

Fig. 5. Variations in the 50% condensation temperatures of elements as a function of pressure.

from previous studies (Canup et al., 2015; Lock et al., 2018; O'Neill, 1991; Visscher and Fegley, 2013), information on trace elements is sparser. However, the speciation is very relevant as it is of importance for constraining the isotope fractionation of these elements during the Moon formation (e.g., Wang et al., 2019). This may play a role in the magnitude of kinetic isotope fractionation that scales as $\sqrt{m}$ where m is the mass of the evaporating species. Similarly, equilibrium isotope fractionation between vapor and melt obviously depends on the nature of the vapor species (e.g., Sossi et al., 2018; Wang et al., 2019). Wang et al. (2019) reported a significant depletion in Sn isotopes in lunar rocks relative to terrestrial rock. As SnO is the stable volatile species while the most abundant form in the melt is Sn, this observation was used to argue that the observed δ^{124}Sn in the Moon resulted from equilibrium isotope fractionation during repeated events of volatile loss. In the case of Cr isotopes, it was shown by Sossi et al. (2018) that the stable vapor species is CrO_2 (Cr is then in the IV oxidation state) while Cr_2O_3 is the main species in the silicate melt in equilibrium with a gas phase. Thus, the oxidation state of Cr in the vapor being higher, the vapor should be enriched in heavy Cr isotopes relative to the condensed phase. Sossi et al. (2018) argued that the bulk Silicate Moon is enriched in light Cr isotopes compared with the bulk Silicate Earth and this could reflect the loss of volatile CrO_2 during Moon formation.

Our calculations show that for many of the trace elements of interest, the atomic vapor is not always the most abundant species (Table S3 and Fig. 6). This is the case for some alkali and transition metals that form oxides or hydroxide molecules that are more abundant than the atomic species (e.g. Sn, Cr, Mo, and W). This is illustrated in Fig. 6 showing the volatile species distribution as a function of temperature at a constant pressure of 10 bar. The mole fraction of the volatile species is a function of temperature and, in some cases, the nature of these species changes with decreasing temperature. Depending on the temperature of vapor-liquid decoupling (that ultimately results in the loss of volatile elements), the pattern of isotope fractionation for these elements may be different. In the case of Cr, it is found that in the presence of H, the most stable species is not CrO_2 as argued by Sossi et al. (2018) but CrOOH. Thus, it is possible that the isotope fractionation will be different from what was predicted by Sossi et al. (2018). Similarly, we show that the most stable species for Sn is SnO as reported in Wang et al. (2019) for temperatures between 2000 and 2500 K. However, at lower temperatures, SnS becomes the most abundant species, assuming the amount of S present is equal to that of the BSE. For Mo, there is an interesting pattern as the most abundant species at high temperature is MoO_2 and then MoO for temperatures below 3000 K followed by $MoO_2(OH)_2$ at temperatures below 2200 K. The elements that have a variable vapor speciation in the conditions of the Moon formation are Cr, Mo, U, Sn, Ge, Cu, Cs, Se, Ti and K, as illustrated in Fig. 6. For all these elements, the pattern of isotope fractionation associated with volatility could be more complex than expected and would deserve closer scrutiny. These calculations illustrate that if isotope fractionation is associated with these changes in speciation, then isotope tracers could be a powerful tool to decipher the P-T conditions of Moon formation.

3.5. *Prediction of elemental abundances in the moon*

Our thermodynamic calculations can be used to predict the abundances of elements in the Moon by assuming a given value of the pressure while the temperature of the protolunar disk cools down. This approach is obviously simplified because the condensation of elements could have taken place over a range of pressures depending on the exact process of vapor-melt separation (Canup et al., 2015; Charnoz and Michaut, 2015; Lock et al., 2018; Machida and Abe, 2004; Nie and Dauphas, 2019). It also depends on the structure and dynamics of the circumplanetary disk that forms after a giant impact. The calculated abundances are then compared with a best estimate for the bulk chemical composition of the Moon. This bulk composition was determined by combining the approaches from various studies. For refractory lithophile elements (RLE), the data from Hauri et al. (2015) was used and it is overall consistent with the recent determinations of Taylor and

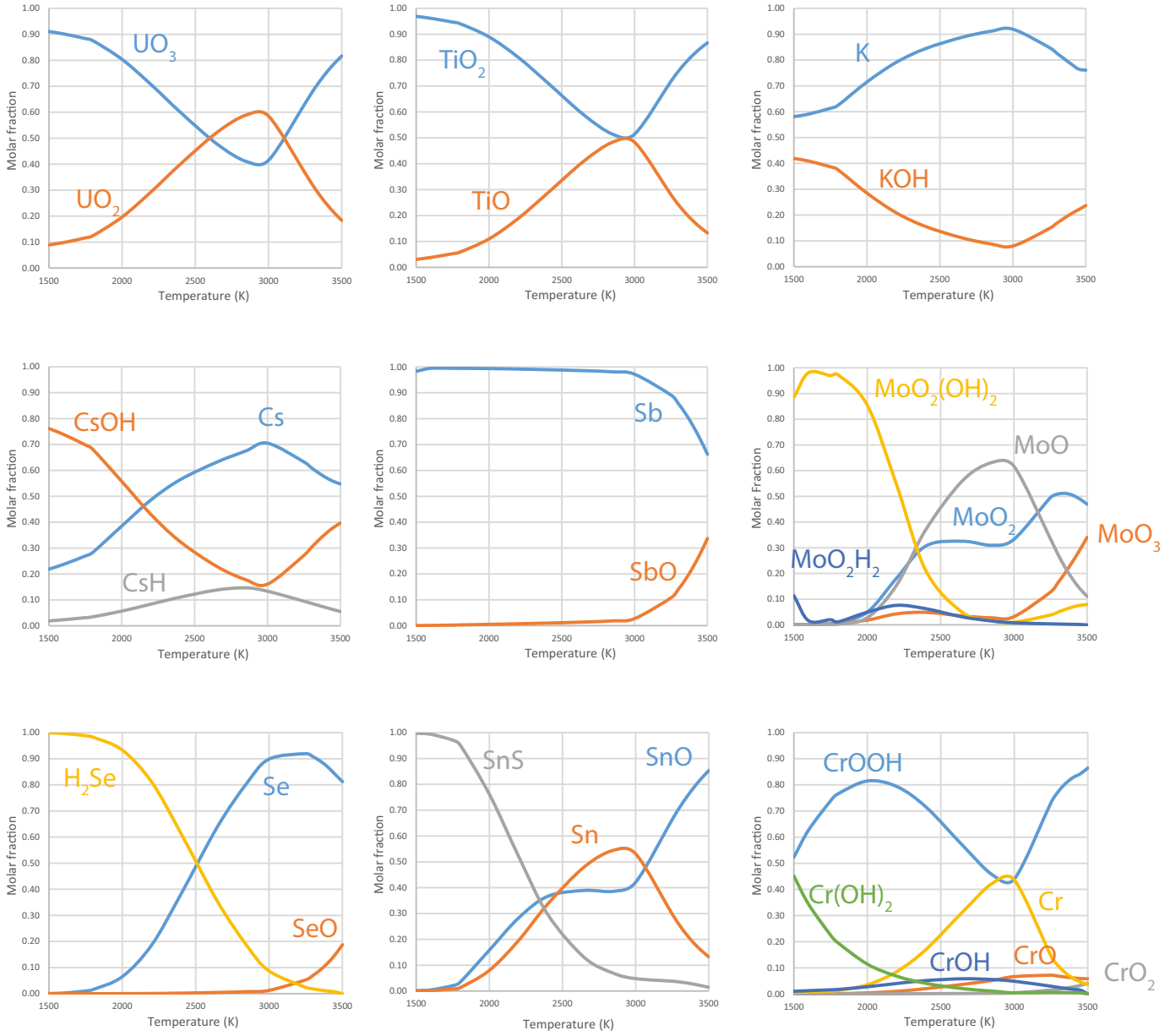

Fig. 6. Speciation of trace elements in the vapor phase as a function of temperature at a pressure of 10 bar.

Wieczorek (2014) who took into account a new evaluation of crustal thickness and the implications for the RLE concentrations in the Moon. For volatile alkali metals, we took the determinations of Taylor and Wieczorek (2014) who used trace element ratios of incompatible elements to estimate their composition in the BSE. Since the lunar core is small, it is then possible to infer directly the concentrations in the bulk Moon. For siderophile elements, Anders et al. (1977), O'Neill (1991) and Righter (2019) have estimated the composition of the bulk Moon, taking into account the budget that must reside in the lunar core. Righter (2019) pointed out that Cu, Ga, Zn are only weakly siderophile and hence their budget in the core is small, in contrast with Sb, Ag, Ge, Sn, Ni, Co which are more siderophile. The best estimate for the bulk Moon composition given in Table 5 reflects all these considerations.

As explained in the next section, the lunar bulk composition resulting from vapor separation were calculated for various structures of protolunar disk (see below) and for the P-T conditions of the disk model of Canup et al. (2015). We also calculated the composition of the condensates for various P-T conditions used to match the lunar composition by Lock et al. (2018). The results of these calculations are shown in Figs. 7 and 8 (see tabulated results in Table S4) and are further discussed below.

3.6. *Pressure conditions of condensation*

The phase diagram shown in Fig. 2 clearly illustrates that for a given temperature there is a broad domain where both the vapor and liquid coexist. For a temperature of 3000 K, there will be vapor+liquid between 2×10^{-2} bar up to an undetermined upper bound higher than 10^{2} bars. Thus, for a given temperature, one cannot uniquely specify the pressure in the protolunar disk a priori. However, the system does not evolve independently of the physics of the disk (Genda and Abe, 2003) or of the synestia (Lock et al., 2018) as the structure of the vapor+liquid mixture should depend on its dynamics. In what follows, we have examined various P-T conditions and calculated the corresponding chemical compositions of condensates in these conditions. For the sake of example, we have first examined an analytical model proposed by Genda and Abe, (2003). If we assume as Genda and Abe (2003) that the vapor+liquid mixture behaves adiabatically since it is convective, then

Table 5
Bulk Moon composition used for comparison with BSE.

Element	Bulk Moon (wt%)	Bulk Moon/BSE
Al	2.35588235	1.00250313
Ca	2.53571429	1.00225861
Ti	0.11578947	0.9609085
W	0.0000017	0.5862069
Mg	22.7925558	0.9996735
Si	21	1.0
Mo	0.0000068	1.36
Mn	0.10457746	1.00074129
Fe	6.25612813	0.99938149
Cr	0.1916	0.72990476
Co	0.0105	1.0
Na	0.08903226	0.33345415
Ni	0.196	1.0
K	0.00567574	0.23648936
Cu	0.00035	0.11666667
Sb	0.00000006	0.10909091
Zn	0.00077	0.01
Sn	0.00000195	0.15
Rb	0.0000147	0.245
Ge	0.000021	0.19090909
Ag	1.8E-08	0.0225
Cs	0.00000067	0.31904762
Se	0.0000024	0.32

one can make some assumptions about the relationship between pressure and density as a function of distance. With this approach, Genda and Abe (2003) have calculated the pressure as a function of distance r and height z assuming a cylindrical symmetry for a rotating object around the Earth. The pressure is considered to be proportional to the power of the radial distance:

$$p_{r,0} = p_{r_E,0}\left(\frac{r}{r_E}\right)^{-\zeta}$$

It is then possible to calculate the pressure as a function of r and z:

$$\frac{p}{p_{0,0}} = \left[\frac{\gamma-1}{\gamma}\lambda\left(\frac{r_E}{\sqrt{r^2+z^2}} - \frac{r_E}{r}\right) + \left(\frac{r_E}{r}\right)^{\zeta\frac{\gamma-1}{\gamma}}\right]^{\frac{\gamma}{\gamma-1}}$$

Where r_E is the radius of the Earth, ζ is a free parameter and γ is polytropic exponent which was calculated to be equal to 1.05 by Genda and Abe (2003). The density can also be deduced from this equation using the gas law:

$$\frac{\rho}{\rho_{0,0}} = \left[\frac{\gamma-1}{\gamma}\lambda\left(\frac{r_E}{\sqrt{r^2+z^2}} - \frac{r_E}{r}\right) + \left(\frac{r_E}{r}\right)^{\zeta\frac{\gamma-1}{\gamma}}\right]^{\frac{1}{\gamma-1}} = f(r,z)$$

The total mass of the disk can be then found from the following integral:

$$M_{disk} = \iint 2\pi r\rho(r,z)drdz = \rho_{0,0}\iint 2\pi r f(r,z)drdz$$

The variable r is integrated from the surface of the Earth r_E to infinity, while z is integrated from 0 to the value where the density goes to zero, which is defined as:

$$z_{max} = \sqrt{\left(r_E\Big/\left(\frac{r_E}{r} - \frac{\gamma}{(\gamma-1)\lambda}\left(\frac{r_E}{r}\right)^{\zeta\frac{\gamma-1}{\gamma}}\right)\right)^2 - r^2}$$

An additional assumption that stems from the general dynamics of the impact is the total mass ejected during the impact, the minimum amount being equal to the mass of the Moon. If we assume for the sake of argument that the ejected mass is that of the Moon, one can calculate the pressure at the surface of the terrestrial magma ocean and then deduce its variation as a function of distance:

$$p_{0,0} = \frac{M_{disk}X^0_{vap}RT_0}{M_{vap}\iint 2\pi r f(r,z)drdz}$$

Where M_{vap} is the mean molar mass of the vapor, R the gas constant, T_0 the temperature at the surface of the magma ocean, and X^0_{vap} is the molar fraction of vapor in the disk.

$$p_{r,0} = \frac{M_{disk}X^0_{vap}RT_0}{M_{vap}\iint 2\pi r f(r,z)drdz} \times \left(\frac{r}{r_E}\right)^{-\zeta}$$

Of particular relevance is the pressure beyond the Roche radius which represents the minimum distance where the Moon can accrete. The distance of 1.7 × R_{Earth} used in Charnoz and Michaut (2015) represents the maximum distance where a continuous layer of liquid can be stable in the disk midplane, while 3 × R_{Earth} is the Roche limit for the existence and stability of a liquid body bound together by its own gravity. Thus, if the condensed material formed at 1.7 × R_{Earth} moves rapidly to 3 × R_{Earth}, the pressure of equilibration may still be 1.7 × R_{Earth}. For the sake of our calculations, we will be using that at 3 × R_{Earth}. This pressure corresponds to the pressure experienced during Moon accretion representative of liquid-vapor separation, if one assumes there is a decoupling of vapor and liquid during the evolution of the disk (Charnoz and Michaut, 2015; Lock et al., 2018; Wang et al., 2019). For each of these pressures, we determined the mass fraction of vapor corresponding to the P and T conditions (as reported in Table S3) and recalculated the corresponding pressure until we reached convergence of the pressure value P_0 (pressure at the surface of the magma ocean). For a range of temperatures corresponding to the overall cooling of the system, one can thus estimate a possible range of pressures at the Roche radius.

For ζ = 4 (protolunar disk with a donut shape, ζ is the parameter used in the model of Genda and Abe (2003), these pressures are different from the P-T relationships estimated by Visscher and Fegley (2013). These values represented the sum of all partial pressures of the vapor constituents in equilibrium with the melt containing all the oxides. However, the pressures calculated by Visscher and Fegley (2013) are better matched if the value of ζ is equal to 2. The value of ζ is intrinsically dependent on the dynamics of the disk and unless this parameter (or more generally the post-impact structure) is fully specified, it is difficult to determine the exact P-T path.

These calculations based on an analytical model of the disk should only be considered as illustrative and show that the P-T conditions depend on the post-impact structure of the disk or synestia. Rather than considering a specific structure, we have explored a wide range of P-T conditions corresponding to those in the literature and calculated the chemical composition of condensates. Our results are thus independent of a particular post-impact model.

3.7. Role of water in shifting of condensation curves

To estimate the influence of water presence on the condensation processes taking place during the Moon formation, we calculated condensation curves with different initial hydrogen concentrations from 0 to 1000 ppm at 1 mbar pressure (Fig. 9) for a BSE composition. Slight decrease in the condensation temperatures with the addition of hydrogen is observed for the more volatile elements: Zn, Cu, S, Ni, K and Na. The most significant temperature shifts can be found for H concentrations >200 ppm: Zn (T_{200ppm} - T_{0ppm}) = -124 K and Cu (T_{200ppm} - T_{0ppm}) = −224 K. The condensation curves of the less volatile metals do not depend on the presence of water. One conclusion of our calculations is that water does not greatly influence the condensation temperatures (within a reasonable range) and therefore this data cannot be used directly to infer the abundance of water in the Moon.

4. Discussion: Implications for the formation of the moon and its chemical composition

Our results for the phase relationships in the proto-lunar disk are overall consistent with the phase diagram given in Lock et al. (2018).

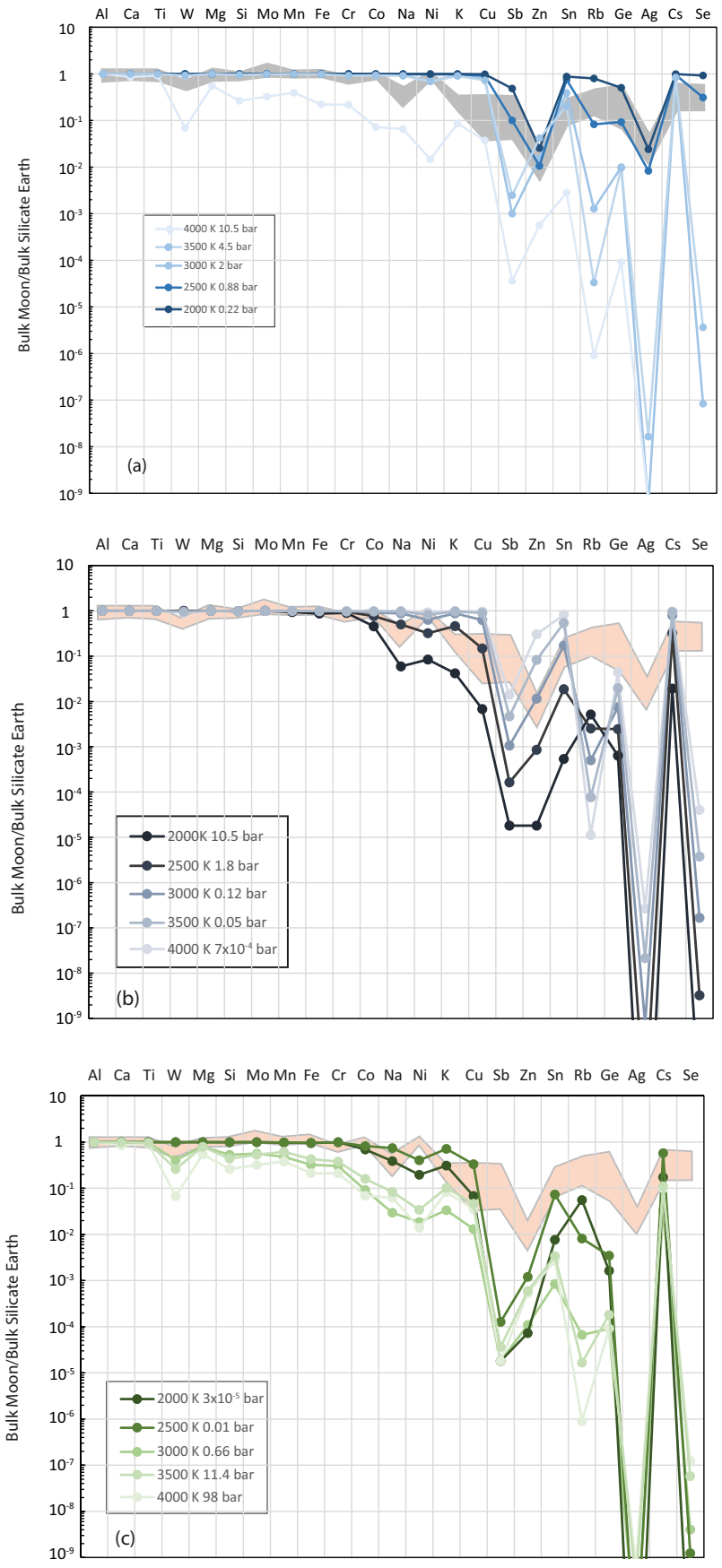

Fig. 7. Calculated composition of the Moon normalized to the BSE composition for the pressure range 1 mbar – 10 bar. The horizontal scale corresponds to elements ordered by their condensation temperatures. (a) P-T conditions calculated with $\zeta = 4$ (b) P-T conditions calculated with $\zeta = 2$ (c) P-T disk conditions of Canup et al. (2015). Bulk Moon composition was estimated based on the work of Hauri et al. (2015), O'Neill, (1991) and Righter (2019) and is reported in Table 5. ζ is the parameter used in the model of Genda and Abe (2003).

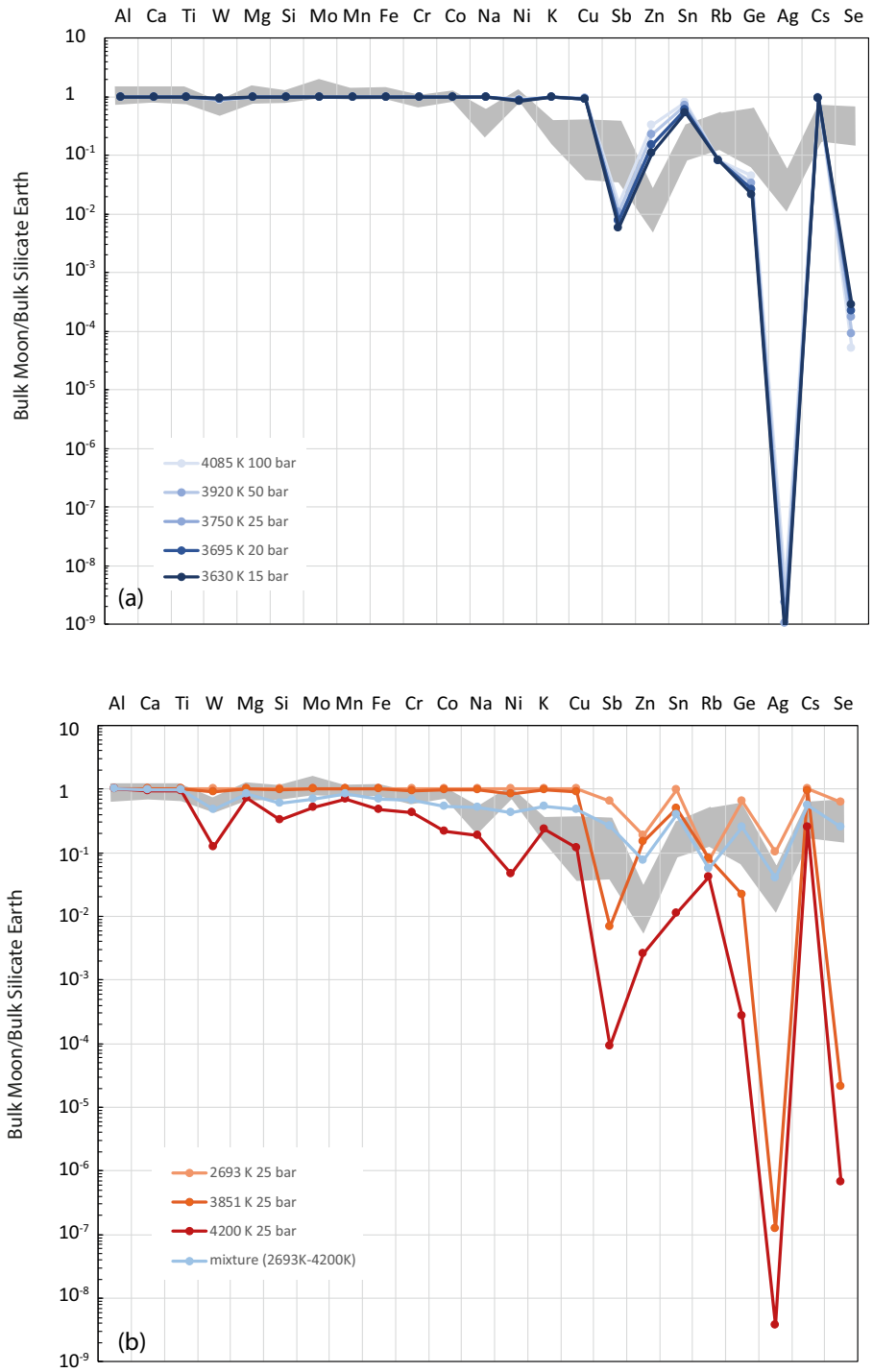

Fig. 8. Calculated composition of the Moon normalized to the BSE composition for the P-T conditions used in Lock et al. (2018) in their Fig. 14 (a) and S4 (b). The corresponding P-T values are given in the diagram. The light blue curve in panel b corresponds to a mixture between the condensate at 2693 K and the condensate at 4200 K. (For interpretation of the references to colour in this figure legend, the reader is referred to the web version of this article.)

There are however, a few differences in the position of phase transitions. Notably, our melt+vapor/vapor line is 200 K higher at 1 bar than that of Lock et al. (2018). The metal condensation line (an Fe—Ni alloy) is also offset towards 200 K higher temperatures at 1 bar with a smaller offset at lower pressures. These discrepancies may be due to the difference in the activity models used for the main constituents or to difference in the thermodynamic data. In fact, the overall predictions of phase boundaries are consistent.

If one attempts to reconstruct the chemical composition of the bulk Moon using a thermodynamic approach, one needs to constrain both the pressure and temperature of vapor-liquid separation. As shown in Section 3.6, it is possible to calculate the pressure and temperature conditions for various models of the proto-lunar disk using simplistic assumptions regarding its structure. However, we have made calculations for a broader range of P-T conditions to be independent from a specific model structure. For the simple analytical model, we have made relevant calculations of the chemical composition of the bulk lunar material assuming single stage melt-vapor separation for two sets of

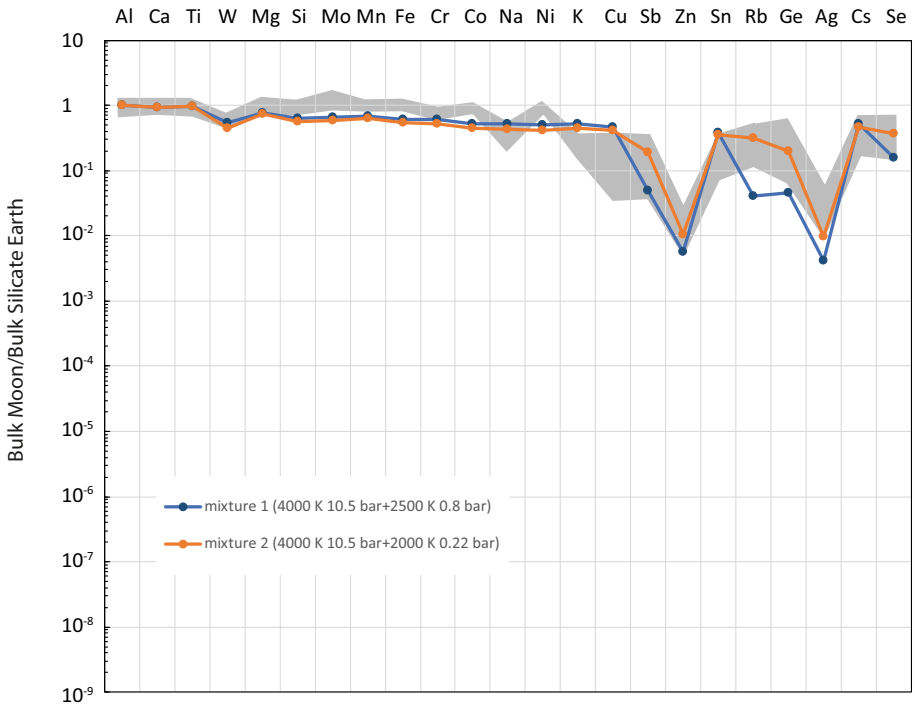

Fig. 9. Dependence of 50% condensation temperature on hydrogen concentration at 1 mbar.

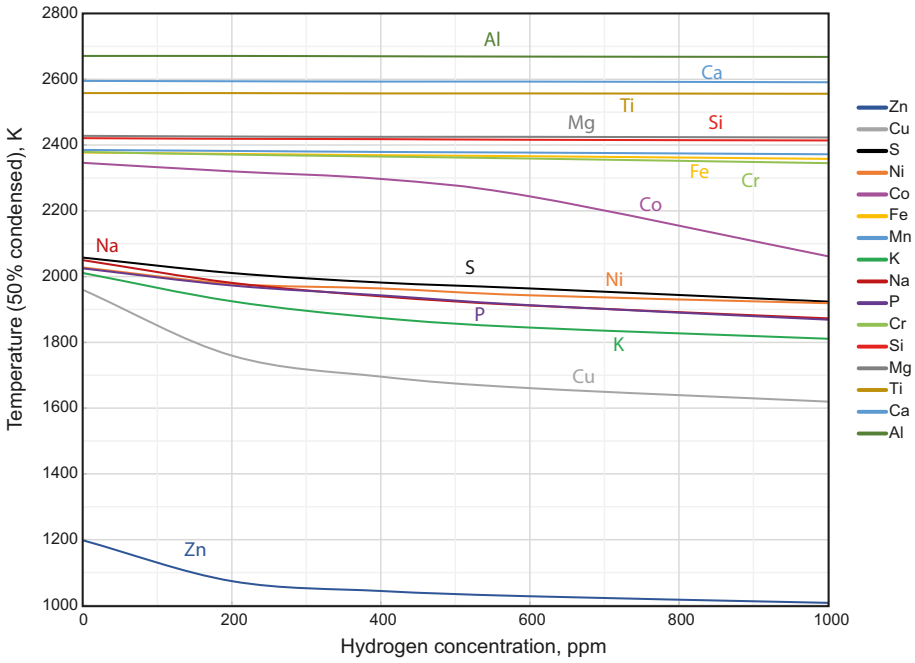

Fig. 10. Calculated composition of the Moon normalized to the BSE composition for mixtures of high temperature and low temperature condensates. Note that these mixtures produced depletion in alkali elements corresponding to the observations.

values of the parameter $\zeta = 2$, and $\zeta = 4$ at the Roche limit, beyond which accretion of the Moon is possible (Fig. 7a–b). The corresponding P-T paths are given in Fig. S4 and can be compared with the P-T conditions used in previous studies (Figs. 7c and 8 (Canup et al., 2015; Lock et al., 2018) for their condensation calculations. Fig. 8 also shows the composition of condensates using the exact P-T conditions used in Lock et al. (2018) to construct their Figs. 14 and S4. For the conditions in Fig. 7b, c (Canup et al., 2015) and 8 (Lock et al., 2018), there is not a good fit of the data to the lunar compositions. The best fit is obtained for $\zeta = 4$, for pressure ranging between 0.8 and 0.22 bar and temperatures between 2500 and 2000 K. For higher temperatures, the concentrations of the most volatile elements are far below those measured in the Moon. One can note, however that the alkali compositions do not fit well even with this model. Thus, one important conclusion is that there is no good fit that matches properly the composition of the Moon using a single P-T couple.

Our results differ from those of Lock et al. (2018) partly because our set of volatile elements extend beyond Ge, which was already shown to

be difficult to fit with the conditions of Lock et al. (2018). In fact, the Ge depletion in the Moon is not thought to be a low as that shown in Fig. 14 of Lock et al. (2018). Rather, Righter (2019) argues that the extreme depletion reported in some lunar rocks is due to Ge volatilization upon eruption (as described in the Lunar Source Book). According to Steenstra et al. (2016) Ge is not even depleted in the bulk Moon. Overall our calculations (Fig. 8) show that the depletion in Se, Ag and Ge would be much greater than those observed if one uses the P-T conditions of Lock et al. (2018). In contrast, if we use our preferred P-T conditions ($\zeta = 4$), one can match the abundance of these elements.

Another important result of our calculation is that the mass fraction of liquid metal represents 0.6 to 0.74% of the condensed mass, which matches remarkably well the mass fraction of the lunar core, according to recent estimates (Kronrod et al., 2020). As the system cools down, the mass fraction of metal should increase and be even more consistent with the lunar core size as given in Kronrod et al. (2020) (~1%) or Williams et al. (2014) (<1.5%). This lends further support that our conditions of condensation are reasonable for explaining the lunar composition.

Thus, an important aspect of our modeling is the role of the liquid metal in controlling the abundance of siderophile volatile elements. If the liquid metal is not present, there is little condensation of these elements in the silicate melt and they remain partitioned in the vapor. The bulk composition of the Moon shows that these elements are not that depleted relative to the BSE as their relative depletion factor ranges between 0.1 and 0.01. Their abundance is thus largely controlled by the appearance of liquid iron+nickel as shown in Fig. 2, which is not possible using the P-T conditions used in Canup et al. (2015) and Lock et al. (2018). Since our model seems to match the Moon abundances for these elements, one can infer that it is important for the condensation to take place while at least part of liquid metal was stable. In detail, the activity coefficients of all these elements are not perfectly known and our calculations are based on experimental data published in the literature. It is likely that these parameters could be off due to variations in compositions or due to extrapolation as some of the experiments were done at lower temperatures. However, the role of metal seems inescapable despite some uncertainties in their activity coefficients, as there is a large gap in the calculated abundance in the silicate melt compared with the iron-nickel liquid.

As mentioned above, the fit for alkali elements (especially Na, Rb and Cs) is poor when considering the conditions that matches siderophile volatile elements. In order to improve this fit, we also considered models where condensates formed at different temperatures could accrete to form the Moon. This would correspond to condensates formed in various locations in the disk structure and having migrated radially as described for example in Lock et al. (2018) or by mixing condensates from different heights in the disk. The composition of a high-T (50–60%) and low-T (40–50%) mixture is shown in Figs. 8b and 10 and the predicted compositions are better than those obtained for a single P-T equilibrium condition. The P-T conditions of the low-T condensate are consistent with those predicted in Wang et al. (2019). Establishing how this mixing of condensates actually took place within the protolunar disk would require a specific physical model that is beyond the scope of this study. These results again emphasize that it is important to have a condensate that has saturated liquid metal in order to match the volatile siderophile element contents while the higher temperature condensates are necessary to match the alkali contents.

5. Conclusions

Our study demonstrates that the elemental abundances in the Moon compared with that of the Earth depend on the pressure and temperature conditions of vapor-liquid separation during the proto-lunar disk phase following the giant impact. It is thus crucial to use the corresponding condensation temperatures and vapor pressures to establish the volatility scale of all elements and, as in previous studies, these temperatures were higher than those calculated for the Solar Nebula.

Our results show that there is not a single set of pressure and temperature that matches all the major and trace element compositions of the Moon. The best fit is obtained for a mixture of high temperature condensate (4000 K, 10.5 bars) with a low temperature condensate (2500-2000 K, 0.8–0.22 bars) in order to match both the siderophile volatile and alkali abundances. In any lunar formation scenario, for the low temperature condensate, it is important that liquid metal is stable, thereby enhancing the abundance of volatile siderophile elements in the condensed phase.

The role of water may be important in controlling the vapor speciation for some elements (e.g. Cr) while many elements are affected by the high oxygen fugacity leading to oxide vapor species (e.g. Mo, W). These considerations are important to model the isotope fractionation of volatile elements between the Moon and bulk Silicate Earth.

Our calculations heavily depend on the activity coefficients of trace elements and these parameters were not always determined for the exact composition relevant to the formation of the Moon. Better determination of these values should enable to refine our results in the future.

Declaration of Competing Interest

None.

Acknowledgements

We thank Armand Gabriel for his help in learning the intricacies of FactSage™ and Arthur Pelton for advice. This project was funded by the ERC Advanced Grant #694819 COSMOKEMS. We thank Simon Lock and one anonymous reviewer for very helpful and constructive comments that greatly helped improve the manuscript.

Appendix A. Supplementary data

Supplementary data to this article can be found online at https://doi.org/10.1016/j.icarus.2022.115143.

References

Abdelouhab, S., Podor, R., Rapin, C., Toplis, M.J., Berthod, P., Vilasi, M., 2008. Determination of Na2O activities in silicate melts by EMF measurements. J. Non-Cryst. Solids 354, 3001–3011. https://doi.org/10.1016/j.jnoncrysol.2007.12.003.

Albarède, F., Albalat, E., Lee, C.-T.A., 2015. An intrinsic volatility scale relevant to the earth and moon and the status of water in the moon. Meteorit. Planet. Sci. 50, 568–577. https://doi.org/10.1111/maps.12331.

Anders, E., Massey, H.S.W., Brown, G.M., Eglinton, G., Runcorn, S.K., Urey, H.C., 1977. Chemical compositions of the Moon, Earth, and eucrite parent body. Philos. Trans. Royal Soc. London. Series A, Math. Phys. Sci. 285, 23–40. https://doi.org/10.1098/rsta.1977.0040.

Bale, C.W., Bélisle, E., Chartrand, P., Decterov, S.A., Eriksson, G., Gheribi, A.E., Hack, K., Jung, I.H., Kang, Y.B., Melançon, J., Pelton, A.D., Petersen, S., Robelin, C., Sangster, J., Spencer, P., Van Ende, M.A., 2016. FactSage thermochemical software and databases, 2010-2016. Calphad: Computer Coupl. Phase Diagrams Thermochem. 54, 35–53. https://doi.org/10.1016/j.calphad.2016.05.002.

Canup, R.M., 2004. Simulations of a late lunar-forming impact. Icarus 168, 433–456. https://doi.org/10.1016/j.icarus.2003.09.028.

Canup, R.M., 2008. Lunar-forming collisions with pre-impact rotation. Icarus 196, 518–538. https://doi.org/10.1016/J.ICARUS.2008.03.011.

Canup, R.M., 2012. Forming a moon with an earth-like composition via a giant impact. Science 1979 (338), 1052–1055. https://doi.org/10.1126/science.1226073.

Canup, R.M., Visscher, C., Salmon, J., Fegley, B., 2015. Lunar volatile depletion due to incomplete accretion within an impact-generated disk. Nat. Geosci. 8, 918–921. https://doi.org/10.1038/ngeo2574.

Carballido, A., Desch, S.J., Taylor, G.J., 2016. Magneto-rotational instability in the protolunar disk. Icarus 268, 89–101. https://doi.org/10.1016/j.icarus.2015.12.042.

Charnoz, S., Michaut, C., 2015. Evolution of the protolunar disk: dynamics, cooling timescale and implantation of volatiles onto the earth. Icarus 260, 440–463. https://doi.org/10.1016/j.icarus.2015.07.018.

Charnoz, S., Sossi, P.A., Lee, Y.N., Siebert, J., Hyodo, R., Allibert, L., Pignatale, F.C., Landeau, M., Oza, A.V., Moynier, F., 2021. Tidal pull of the Earth strips the proto-Moon of its volatiles. Icarus 364, 114451. https://doi.org/10.1016/J.ICARUS.2021.114451.

Ćuk, M., Stewart, S.T., 2012. Making the moon from a fast-spinning earth: a giant impact followed by resonant despinning. Science 1979 (338), 1047–1052. https://doi.org/10.1126/science.1225542.

Cuk, M., Hamilton, D.P., Lock, S.J., Stewart, S.T., 2016. Tidal evolution of the Moon from a high-obliquity, high-angular-momentum Earth. Nature 539, 402–406. https://doi.org/10.1038/NATURE19846.
Day, J.M.D., Moynier, F., 2014. Evaporative fractionation of volatile stable isotopes and their bearing on the origin of the Moon. Philos. Trans. R. Soc. A Math. Phys. Eng. Sci. 372 https://doi.org/10.1098/rsta.2013.0259.
Dhaliwal, J.K., Day, J.M.D., Moynier, F., 2018. Volatile element loss during planetary magma ocean phases. Icarus 300, 249–260. https://doi.org/10.1016/j.icarus.2017.09.002.
Gammie, C.F., Liao, W.-T., Ricker, P.M., 2016. A hot big bang theory: magnetic fields and the early evolution of the protolunar disk. Astrophys. J. 828, 58. https://doi.org/10.3847/0004-637x/828/1/58.
Genda, H., Abe, Y., 2003. Modification of a proto-lunar disk by hydrodynamic escape of silicate vapor. Earth Planets Space 55, 53–57. https://doi.org/10.1186/BF03352462.
Hauri, E.H., Saal, A.E., Rutherford, M.J., van Orman, J.A., 2015. Water in the moon's interior: truth and consequences. Earth Planet. Sci. Lett. 409, 252–264. https://doi.org/10.1016/j.epsl.2014.10.053.
Kato, C., Moynier, F., 2017. Gallium isotopic evidence for extensive volatile loss from the moon during its formation. Sci. Adv. 3 https://doi.org/10.1126/sciadv.1700571.
Kato, C., Moynier, F., Valdes, M.C., Dhaliwal, J.K., Day, J.M.D., 2015. Extensive volatile loss during formation and differentiation of the moon. Nat. Commun. 6 https://doi.org/10.1038/ncomms8617.
Kronrod, E., Kuskov, O., Matsumoto, K., Kronrod, V., 2020. Estimation of the probable size of the lunar core based on geophysical and geochemical data. In: Journal of Physics: Conference Series. IOP Publishing Ltd, p. 12024. https://doi.org/10.1088/1742-6596/1705/1/012024.
Lock, S.J., Stewart, S.T., 2017. The structure of terrestrial bodies: impact heating, corotation limits, and synestias. J. Geophys. Res. Planets 122, 950–982. https://doi.org/10.1002/2016JE005239.
Lock, S.J., Stewart, S.T., Petaev, M.I., Leinhardt, Z., Mace, M.T., Jacobsen, S.B., Cuk, M., 2018. The origin of the moon within a terrestrial synestia. J. Geophys. Res. Planets 123, 910–951. https://doi.org/10.1002/2017JE005333.
Lodders, K., 2003. Solar system abundances and condensation temperatures of the elements. Astrophys. J. 591, 1220–1247. https://doi.org/10.1086/375492.
Machida, R., Abe, Y., 2004. The evolution of an impact-generated partially vaporized circumplanetary disk. Astrophys. J. 617, 633–644. https://doi.org/10.1086/425209.
Mathieu, R., Khedim, H., Libourel, G., Podor, R., Tissandier, L., Deloule, E., Faure, F., Rapin, C., Vilasi, M., 2008. Control of alkali-metal oxide activity in molten silicates. J. Non-Cryst. Solids 354, 5079–5083. https://doi.org/10.1016/j.jnoncrysol.2008.07.004.
McDonough, W.F., Sun, S.-S., 1995. The composition of the Earth. Chem. Geol. 120, 223–253. https://doi.org/10.1016/0009-2541(94)00140-4.
Mougel, B., Moynier, F., Göpel, C., 2018. Chromium isotopic homogeneity between the Moon, the Earth, and enstatite chondrites. Earth Planet. Sci. Lett. 481, 1–8. https://doi.org/10.1016/J.EPSL.2017.10.018.
Nakajima, M., Stevenson, D.J., 2014. Investigation of the initial state of the Moon-forming disk: Bridging SPH simulations and hydrostatic models. Icarus 233, 259–267. https://doi.org/10.1016/j.icarus.2014.01.008.
Nakajima, M., Stevenson, D.J., 2018. Inefficient volatile loss from the Moon-forming disk: reconciling the giant impact hypothesis and a wet Moon. Earth Planet. Sci. Lett. 478, 117–126. https://doi.org/10.1016/j.epsl.2018.01.026.
Nie, N.X., Dauphas, N., 2019. Vapor drainage in the protolunar disk as the cause for the depletion in volatile elements of the moon. Astrophys. J. 884, L48. https://doi.org/10.3847/2041-8213/ab4a16.
Norris, C.A., 2016. Volatilities of Trace Elements in Silicate Melts, PhD Thesis. University of Oxford.
O'Neill, H.S.C., 1991. The origin of the moon and the early history of the earth-A chemical model. Part 1: the moon. Geochim. Cosmochim. Acta 55, 1135–1157. https://doi.org/10.1016/0016-7037(91)90168-5.
Pahlevan, K., Karato, S. Ichiro, Fegley, B., 2016. Speciation and dissolution of hydrogen in the proto-lunar disk. Earth Planet. Sci. Lett. 445, 104–113. https://doi.org/10.1016/j.epsl.2016.04.015.
Paniello, R.C., Day, J.M.D., Moynier, F., 2012. Zinc isotopic evidence for the origin of the Moon. Nature 490, 376–379. https://doi.org/10.1038/nature11507.
Prettyman, T.H., Hagerty, J.J., Elphic, R.C., Feldman, W.C., Lawrence, D.J., McKinney, G.W., Vaniman, D.T., 2006. Elemental composition of the lunar surface: analysis of gamma ray spectroscopy data from Lunar Prospector. J. Geophys. Res. Planets 111. https://doi.org/10.1029/2005JE002656.
Pringle, E.A., Moynier, F., 2017. Rubidium isotopic composition of the Earth, meteorites, and the Moon: evidence for the origin of volatile loss during planetary accretion. Earth Planet. Sci. Lett. 473, 62–70. https://doi.org/10.1016/j.epsl.2017.05.033.
Righter, K., 2019. Volatile element depletion of the moon—the roles of precursors, post-impact disk dynamics, and core formation. Science. Advances 5, eaau7658. https://doi.org/10.1126/sciadv.aau7658.
Rufu, R., Canup, R.M., 2020. Tidal evolution of the evection resonance/quasi-resonance and the angular momentum of the earth-moon system. J. Geophys. Res. Planets 125, e2019JE006312. https://doi.org/10.1029/2019JE006312.
Schuster, W., Ipser, H., Komarek, K.L., 1979. Thermodynamic properties of iron-selenium alloys. Monatsh. Chem. 110, 1171–1188. https://doi.org/10.1007/BF00910964.
Sossi, P.A., Moynier, F., Van Zuilen, K., 2018. Volatile Loss Following Cooling and Accretion of the Moon Revealed by Chromium Isotopes, p. 115. https://doi.org/10.1073/pnas.1809060115.
Sossi, P.A., Klemme, S., O'Neill, H.S.C., Berndt, J., Moynier, F., 2019. Evaporation of moderately volatile elements from silicate melts: experiments and theory. Geochim. Cosmochim. Acta 260, 204–231. https://doi.org/10.1016/j.gca.2019.06.021.
Steenstra, E.S., Rai, N., Knibbe, J.S., Lin, Y.H., van Westrenen, W., 2016. New geochemical models of core formation in the Moon from metal-silicate partitioning of 15 siderophile elements. Earth Planet. Sci. Lett. 441, 1–9. https://doi.org/10.1016/j.epsl.2016.02.028.
Tang, H., Young, E.D., 2020. Evaporation from the lunar Magma Ocean was not the mechanism for fractionation of the Moon's moderately volatile elements. Planet. Sci. J. 1, 49. https://doi.org/10.3847/psj/abb23c.
Tao, L.C., 1969. Clapeyron equation of a multicomponent solution. Aiche J. 15 (3), 460. https://doi.org/10.1002/aic.690150329.
Taylor, G.J., Wieczorek, M.A., 2014. Lunar bulk chemical composition: a post-gravity recovery and interior laboratory reassessment. Philos. Trans. R. Soc. A Math. Phys. Eng. Sci. 372 https://doi.org/10.1098/rsta.2013.0242.
Tian, Z., Wisdom, J., Elkins-Tanton, L., 2017. Coupled orbital-thermal evolution of the early earth-moon system with a fast-spinning earth. Icarus 281, 90–102. https://doi.org/10.1016/j.icarus.2016.08.030.
Tsukihashi, F., Kuroda, K., Arakawa, S., Sano, N., 1994. Activity coefficient of antimony and arsenic in molten iron and carbon saturated iron. Steel Res. 65, 53–57. https://doi.org/10.1002/srin.199400926.
Visscher, C., Fegley, B., 2013. Chemistry of impact-generated silicate melt-vapor debris disks. Astrophys. J. Lett. 767 https://doi.org/10.1088/2041-8205/767/1/L12.
Wang, K., Jacobsen, S.B., 2016. Potassium isotopic evidence for a high-energy giant impact origin of the moon. Nature 538, 487–490. https://doi.org/10.1038/nature19341.
Wang, X., Fitoussi, C., Bourdon, B., Fegley, B., Charnoz, S., 2019. Tin isotopes indicative of liquid–vapour equilibration and separation in the Moon-forming disk. Nat. Geosci. 12, 707–711. https://doi.org/10.1038/s41561-019-0433-4.
Williams, J.G., Konopliv, A.S., Boggs, D.H., Park, R.S., Yuan, D.N., Lemoine, F.G., Goossens, S., Mazarico, E., Nimmo, F., Weber, R.C., Asmar, S.W., Jay Melosh, H., Neumann, G.A., Phillips, R.J., Smith, D.E., Solomon, S.C., Watkins, M.M., Wieczorek, M.A., Andrews-Hanna, J.C., Head, J.W., Kiefer, W.S., Matsuyama, I., McGovern, P.J., Jeffrey Taylor, G., Zuber, M.T., 2014. Lunar interior properties from the GRAIL mission. J. Geophys. Res. Planets 119, 1546–1578. https://doi.org/10.1002/2013JE004559.
Wisdom, J., Tian, Z., 2015. Early evolution of the Earth–Moon system with a fast-spinning Earth. Icarus 256, 138–146. https://doi.org/10.1016/j.icarus.2015.02.025.
Wood, B.J., Smythe, D.J., Harrison, T., 2019. The condensation temperatures of the elements: a reappraisal. Am. Mineral. 104, 844–856. https://doi.org/10.2138/am-2019-6852CCBY.
Xiao, B., Stixrude, L., 2018. Critical vaporization of MgSiO3. Proc. Natl. Acad. Sci. 115, 5371–5376. https://doi.org/10.1073/PNAS.1719134115.
Young, E.D., Kohl, I.E., Warren, P.H., Rubie, D.C., Jacobson, S.A., Morbidelli, A., 2016. Oxygen isotopic evidence for vigorous mixing during the Moon-forming giant impact. Science 1979 (351), 493–496. https://doi.org/10.1126/science.aad0525.
Zhang, J., Dauphas, N., Davis, A.M., Leya, I., Fedkin, A., 2012. The proto-earth as a significant source of lunar material. Nat. Geosci. 5, 251–255. https://doi.org/10.1038/ngeo1429.